AGU ADVANCING EARTH AND SPACE SCIENCES

JGR Solid Earth

RESEARCH ARTICLE
10.1029/2023JB028110

Mantle Flow Induced by the Interplay of Downgoing Slabs Revealed by Seismic Anisotropy Beneath the Sula Block in Eastern Indonesia

Lingmin Cao[1,2], ChuanChuan Lü[3], Xiaobo He[4], Nicholas Rawlinson[3], Tianyao Hao[5,6,7], Sri Widiyantoro[8,9], Pepen Supendi[3,10], Liang Zhao[6,11], Huaiyu Yuan[12,13], Minghui Zhao[1,2,6], Xuelin Qiu[1,2,6], Muhammad Taufiq Rafie[14,15], Alfian Alfian[16], and David Prambudi Sahara[8]

[1]Key Lab of Ocean and Marginal Sea Geology, South China Sea Institute of Oceanology, Chinese Academy of Sciences, Beijing, China, [2]Southern Marine Science and Engineering Guangdong Lab (Guangzhou), Guangzhou, China, [3]Bullard Labs, Department of Earth Sciences, University of Cambridge, Cambridge, UK, [4]Department of Ocean Exploration and Technology, Zhejiang Ocean University, Zhoushan, China, [5]Key Lab of Petroleum Resources Research, Institute of Geology and Geophysics, Chinese Academy of Sciences, Beijing, China, [6]University of Chinese Academy of Sciences, Beijing, China, [7]Key Lab of Submarine Geosciences, Second Institute of Oceanography, Ministry of Natural Resources, Hangzhou, China, [8]Global Geophysics Research Group, Faculty of Mining and Petroleum Engineering, Institut Teknologi Bandung, Bandung, Indonesia, [9]Faculty of Engineering, Maranatha Christian University, Bandung, Indonesia, [10]Agency for Meteorology, Climatology, and Geophysics, Jakarta, Indonesia, [11]State Key Lab of Lithospheric Evolution, Institute of Geology and Geophysics, Chinese Academy of Sciences, Beijing, China, [12]ARC Centre of Excellence for Core to Crust Fluid Systems, Department of Earth and Environmental Sciences, Macquarie University, Sydney, NSW, Australia, [13]Centre for Exploration Targeting, University of Western Australia, Perth, WA, Australia, [14]Geophysical Engineering Department, Faculty of Mining and Petroleum Engineering, Institut Teknologi Bandung, Bandung, Indonesia, [15]Department of Geophysics, Faculty of Mathematics and Natural Sciences, Hasanuddin University, Makassar, Indonesia, [16]Seismology Exploration and Engineering Research Group, Faculty of Mining and Petroleum Engineering, Institut Teknologi Bandung, Bandung, Indonesia

Abstract The North Sulawesi subduction zone is characterized by southward subduction of the Celebes Sea slab to a depth of ~250 km, mainly overlying the Sangihe slab that subducts west from the Molucca Sea and penetrates the mantle transition zone. The palaeo-subducted Sula slab dips northward and partially underlies both the Sangihe and Celebes Sea slabs. Adjacent subduction zones with horizontal overlapping subducting slabs in the upper mantle have unclear dynamic interactions. An extensive strike-slip fault forms the western boundary of the active North Sulawesi subduction zone, providing an ideal setting to study mantle flow between overlapping slabs. We use local S-wave and teleseismic S and SK(K)S waveform splitting analysis to measure seismic anisotropy in the northern Sulawesi region. Our observations reveal typical mantle wedge corner flow within the Sangihe subduction system. In the Gulf of Tomini, the observed trench-oblique fast-axis orientations above the Celebes Sea slab are likely a consequence of the interaction between two subducting slabs. The southernmost measurement with an E–W-trending fast direction in the mantle wedge might be related to the subduction of the Sula slab. Furthermore, fault-parallel fast-axis orientations of anisotropy near the southern segment of the Palu-Koro fault are attributed to large-scale shearing across this lithospheric-scale strike-slip fault system. Overall, our observations suggest that the strain caused by lithospheric and asthenospheric deformation is mainly confined within the microplate, displaying a restricted flow pattern and localized effects due to the size of the plate boundaries, such as the Palu-Koro fault.

Plain Language Summary North Sulawesi is bordered by the Makassar Strait, Celebes Sea, Molucca Sea, and Gulf of Tomini and hosts the Palu-Koro fault. The region hosts two active subduction zones: the smaller, southward dipping North Sulawesi subduction zone and the larger westward dipping Sangihe subducting slab. Another fossilized submerged slab –Sula slab lies beneath both the Celebes Sea and Sangihe slabs to the south. Thus, it is an ideal area to investigate how the interaction between neighboring subduction zones can affect the upper-mantle deformation and whether a strike-slip fault could contribute to the mantle dynamics. We use shear-wave splitting analysis to measure seismic anisotropy to reveal the lithospheric deformation and upper mantle flow patterns of this interactive area. Our results show that the Celebes Sea slab controls mantle wedge dynamics in the North Sulawesi subduction zone, and the interaction

Key Points:

- We employ shear-wave splitting analysis to characterize the seismic anisotropy to infer upper-mantle deformation in north Sulawesi
- We find evidence for slab-slab dynamic interactions and constrain their influencing spatial range
- The Palu-Koro fault marks the west limit of lithospheric deformation imposed by the complex subduction system

Supporting Information:

Supporting Information may be found in the online version of this article.

Correspondence to:

L. Cao, C. Lü and X. He,
cao_lingmin@126.com;
chuanchuanlu@esc.cam.ac.uk;
xiaobo.he@zjou.edu.cn

Citation:

Cao, L., Lü, C., He, X., Rawlinson, N., Hao, T., Widiyantoro, S., et al. (2024). Mantle flow induced by the interplay of downgoing slabs revealed by seismic anisotropy beneath the Sula Block in eastern Indonesia. *Journal of Geophysical Research: Solid Earth*, *129*, e2023JB028110. https://doi.org/10.1029/2023JB028110

Received 19 OCT 2023
Accepted 4 MAY 2024

Author Contributions:

Conceptualization: Lingmin Cao, Xiaobo He
Data curation: Alfian Alfian
Funding acquisition: Lingmin Cao, ChuanChuan Lü, Tianyao Hao
Investigation: Nicholas Rawlinson, Tianyao Hao
Methodology: Lingmin Cao
Resources: ChuanChuan Lü, Nicholas Rawlinson, Tianyao Hao, Sri Widiyantoro, Pepen Supendi, Muhammad Taufiq Rafie, David Prambudi Sahara
Supervision: Xiaobo He
Validation: ChuanChuan Lü, Nicholas Rawlinson, Sri Widiyantoro, Pepen Supendi, Liang Zhao, Huaiyu Yuan, Minghui Zhao, Xuelin Qiu
Writing – original draft: Lingmin Cao

Writing – review & editing: ChuanChuan Lü, Xiaobo He, Nicholas Rawlinson, Liang Zhao, Huaiyu Yuan, Minghui Zhao, Xuelin Qiu

between the Celebes Sea and Sangihe slabs occurs where two slabs entirely overlap. The strike-slip fault at the western boundary only appears to have a local influence on the regional strain field in western Sulawesi.

1. Introduction

The co-existence of multiple subduction zones in the neighborhood of a triple junction is often observed, such as in the Mediterranean Sea (e.g., Király, Faccenna, & Funiciello, 2018; Vignaroli et al., 2008), Taiwan Orogeny (Király et al., 2016; Lallemand et al., 2001), the Molucca Sea (e.g., Hall & Spakman, 2015; Király, Holt, et al., 2018), Central Japan Island (e.g., Hall, 2002; Ji et al., 2017) and North Sulawesi Island (e.g., Dong et al., 2022; Hall & Spakman, 2015). The dynamic interaction among multiple subducting slabs of different orientations across a range of depths can significantly affect the development of a subduction zone, for example, by relaying stress through the downgoing slab to the upper mantle and the overlying plate. It affects many aspects of the subduction process, such as the intensity of upper plate deformation, the trench migration rate and the upper mantle flow direction (e.g., Dong et al., 2022; Jagoutz et al., 2015; Király et al., 2016, 2021). Beneath North Sulawesi, the interaction between downgoing slabs in the upper mantle is likely a key driver in forming its complex and unique geology. Moreover, one of the most active faults in the Sulawesi region—the Palu-Koro fault, between the North Sula block and the Makassar block, is a left-lateral strike-slip fault. It helps accommodate the NNW migration and the clockwise rotation of the North Sula block and the anticlockwise rotation of the Makassar Block (Socquet et al., 2006). Numerical modeling studies show that two downgoing slabs from two directions strongly influence upper mantle flow, thus generates different trench retreat rates in the study region (Dong et al., 2022).

The North Sula block lies in a tectonically complex area where subduction interaction is associated with the southward-subducting Celebes Sea slab and the westward-subducting Sangihe slab (Figure 1). The Celebes Sea slab (CSS) overlies the Sangihe slab (SHS), with the former penetrating to a depth of ∼250 km, and the latter to at least the base of the mantle transition zone based on several regional seismic tomography images (Greenfield et al., 2021; Hayes et al., 2018; Wehner et al., 2022; Zenonos et al., 2019). SHS forms the oldest active subduction zone along the Indonesia-Philippine Sea plate boundary, which features a dip angle of 55–65° in the mantle (Cardwell et al., 1980; Tatsumi et al., 1991; Zenonos et al., 2019) since ∼25 Ma (Jaffe et al., 2004). According to previous studies, SHS produces a large mantle wedge, which forms the dominant mantle flow above the 660 km discontinuity in the region (Cao et al., 2021; Di Leo et al., 2012a, 2012b). In contrast, the overlying CSS has been thrust beneath the north arm of Sulawesi Island from the North Sulawesi trench, which is only ∼5 Ma (e.g., Hall & Spakman, 2015; Kopp et al., 1999). The relocation of intraslab earthquakes and seismic tomographic images suggest that the two slabs collide at a depth of ∼200 km (Cottam et al., 2011; Hall & Spakman, 2015). Last but not least, the Sula slab (SLS), a northward dipping and fully submerged subduction slab (i.e., it is not connected to the lithosphere at the surface), is present in the southern neighborhood of the North Sula block. It resides above the 660 km mantle discontinuity, leading to a further complicated tectonic setting (e.g., Hall & Spakman, 2015; Figure 1).

Even a first-order understanding of the regional upper-mantle dynamics beneath the study area is lacking due to the availability of limited seismic observations. Previous studies mainly relied on data from a few permanent seismic stations of the Indonesian network without restricted access (Cao et al., 2021; Di Leo et al., 2012a, 2012b), thus limiting their discussion to the dynamics induced by a single subducting slab, and leaving the critical question of slab-slab interactions unaddressed. Furthermore, the role of the Palu-Koro fault (PKF), which marks the boundary between the North Sula and Makassar blocks (Natawidjaja et al., 2021), in influencing regional upper-mantle deformation is yet to be investigated. This study employs shear-wave splitting techniques on teleseismic and local earthquake data. We aim to characterize lithosphere and upper mantle deformation associated with the subducting CSS, SHS, SLS, and PKF, thereby advancing our understanding of dynamic mantle interactions between subducting slabs and interactions between subducting slabs and major continental strike-slip faults.

2. Data and Method

When traveling within an anisotropic layer, a shear wave splits into two orthogonal quasi-shear waves propagating at different speeds. Two splitting parameters, that is, the fast wave polarization direction (φ) and the delay

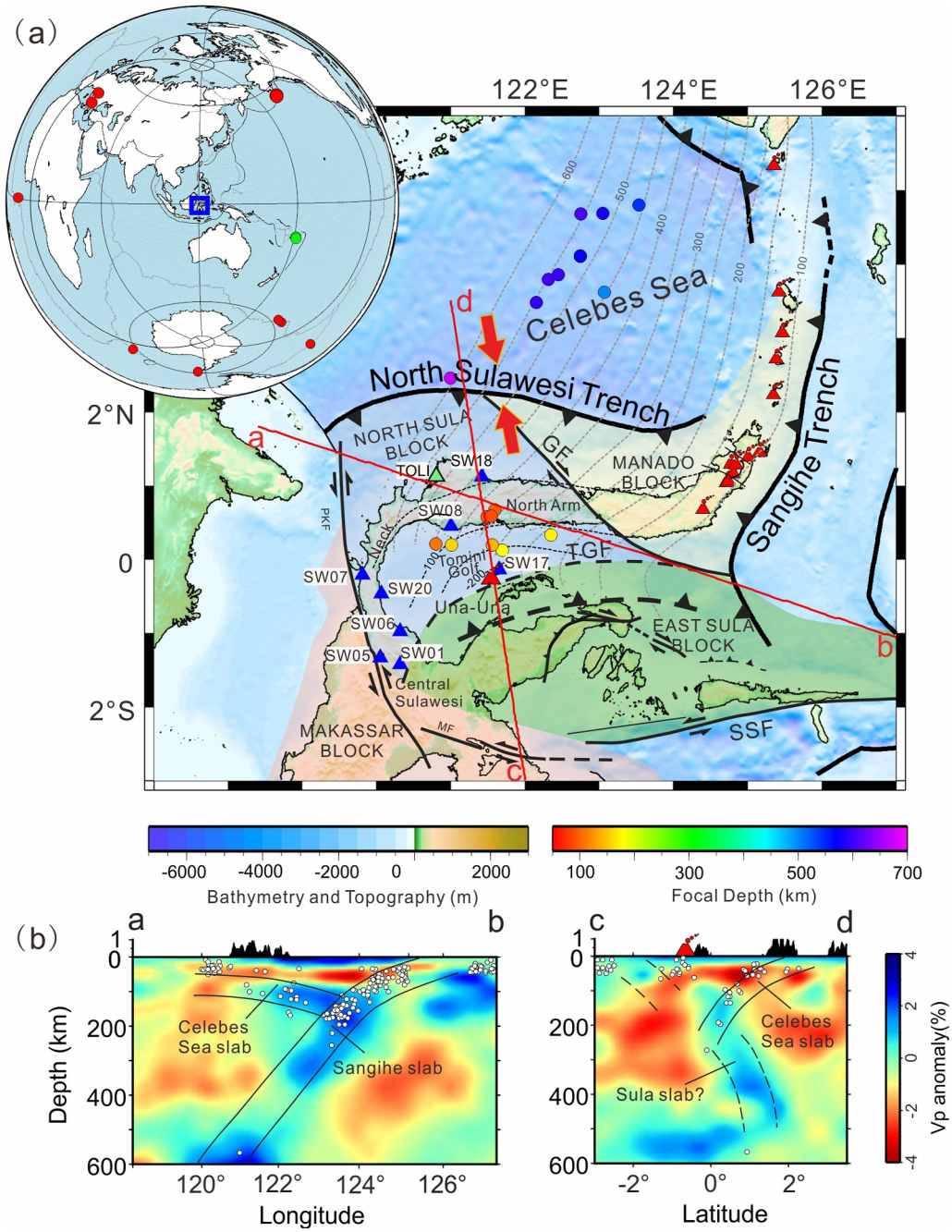

Figure 1. (a) Regional topographic and bathymetric map that shows the location of one permanent (green triangle) and eight temporary (blue triangles) broadband seismic stations, along with various tectonic features. Local earthquakes are denoted by colored circles. Red triangles are Quaternary volcanoes. The gray contour lines show the depths to the upper boundaries of the downgoing slabs with an interval of 50 km, based on SLAB2 (Hayes et al., 2018). The thick dashed line with black triangles shows the inferred trench location of the fully submerged Sula slab (Hall & Spakman, 2015). Pink arrow pair indicates convergence directions between plates or micro-plates on both sides of the trenches (Liu & Shi, 2021). PKF, Palu-Koro fault; MF, Matano fault; GF, Gorontalo fault; SSF, Sula-Sorong fault; TGF, Tomini Gulf fault, which is a fault inferred by a GPS velocity study (Socquet et al., 2006). Translucent shaded regions indicate the ranges of microblocks in and around the Sula Block (modified from Socquet et al., 2006). Red lines denote the locations of velocity perturbation cross section shown in (b). In the top left inset map, red and green circles show Mw > 6.0 teleseismic events used in the final *SKS*- and *S*-phase splitting analysis respectively, and the blue rectangle indicates the study area. (b) *Vp* perturbations in tomographic models by Amaru (2007). In general, the red and blue colors represent low and high *Vp* perturbations, respectively, whose scale is shown at the right. White dots show earthquakes spanning from 1990 to 2020 with magnitude >5 (the catalog is from USGS) that occurred within a 20-km width along each profile.

Table 1
Station Information

Station	Lon (°)	Lat (°)
SW01	120.315	−1.426
SW05	120.049	−1.33
SW06	120.319	−0.977
SW07	119.811	−0.21
SW08	121.001	0.452
SW17	121.653	−0.1362
SW18	121.414	1.117
SW20	120.062	−0.469
TOLI	120.794	1.121

time (δt) between the fast and slow waves, are commonly used to characterize seismic anisotropy. As shear wave splitting has grown in popularity as a tool for measuring seismic anisotropy, different packages for splitting analysis have been developed. In this study, we used the multiple frequency automatic splitting technique software package (MFAST; Savage et al., 2010; Teanby et al., 2004; Wessel, 2010) on the local and teleseismic *S* waves to determine φ and δt. MFAST builds upon the eigenvalue method (Silver & Chan, 1991) and conducts an automatic grid search for a best-fitting solution by incremental shifting the analysis window within a specified waveform segment. This method aims to identify φ and δt, and the initial *S* wave polarization prior to splitting can be found as part of this process. Therefore, it is suitable for local S waves. For the *SK(K)S* waves, we additionally applied the SplitLab toolkit (Wüstefeld et al., 2008). SplitLab offers three different methods: the rotation correlation method (RC, Bowman & Ando, 1987), the minimum energy method (SC, Silver & Chan, 1991), and the eigenvalue method (EV, Silver & Chan, 1991).

We assembled local *S* and teleseismic *S* and *SK(K)S* waveform data from eight temporary and one permanent three-component broadband seismographs in and around the North Sula block for the purpose of shear wave splitting analysis (the fast polarization direction φ and delay time δt) (e.g., Silver & Chan, 1991). The University of Cambridge and the Institut Teknologi Bandung (ITB) deployed the temporary broadband stations between November 2019 and March 2021. The permanent station (TOLI) forms part of the Indonesian national seismic network, and in this case the data is in public domain. Three stations are located on the northern arm of Sulawesi, one near Una-Una volcano, and five on the <50 km wide land bridge that connects the north arm to central Sulawesi (Table 1 and Figure 1). The earthquake catalog used for event location, origin time and magnitude is provided by the National Earthquake Information Center (NEIC). To characterize upper-mantle deformation, the events used for local *S* phase splitting are limited to magnitude Mb > 4.0 recorded at stations within a 35° cone of incidence angles (i.e., the so-called "shear wave window"; Booth & Crampin, 1985). For teleseismic *S* and *SK(K)S* wave splitting, the events are limited to Mw > 5.5 recorded with epicentral distances of 60° to 85° and 85° to 135°, respectively. Furthermore, only events deeper than 420 km were used for teleseismic *S*-wave splitting measurements to minimize source-side anisotropy in the upper mantle. Teleseismic data recorded by the permanent station TOLI have been exploited in several previous *SKS* splitting studies Di Leo et al. (2012a) and Cao et al. (2021); here we retrieve data spanning from the period 2009 to 2019 for local *S* splitting analysis. The teleseismic splitting results from the previous studies noted above are also included in our subsequent analysis.

The signal-to-noise ratio (SNR) of the shear waves is defined by the ratio of the maximum amplitude of the signal on the radial component inside the measurement window and the 2σ value of the amplitude on the tangential component within the same measurement window (Restivo & Helffrich, 1999). We first band-pass filtered the original broadband waveforms between 0.02 and 0.2 Hz for the teleseismic *S* and *SK(K)S* and 0.1–1 Hz for the local *S* phases, respectively, to enhance the SNR of the shear waves, with the exception for station SW17 where the filter was between 0.04 and 0.15 Hz for *SKS* due to relatively poor SNR. Station SW17 is located on the backarc of the North Sulawesi subduction zone, whose results are critical in constraining the mantle deformation related to the inward dipping double-sided subduction of the Celebes Sea and Sula slabs. Due to the coastal basement lithology of the deployment area, the seismic waveforms are typically quite noisy (Cao et al., 2021; Di Leo et al., 2012a, 2012b). We carefully inspected all waveforms manually, and only used the data with SNR greater than 3. We then used the MFAST program (Savage et al., 2010; Teanby et al., 2004; Wessel, 2010) to constrain the anisotropic seismic parameters φ and δt. Following the procedures described in Teanby et al. (2004) and Wüstefeld et al. (2008), only those results which match the following criteria are retained: (a) minimal energy on the transverse component of *SK(K)S* waves or on the perpendicular component of incoming polarization direction for local/teleseismic *S* waves; (b) good correlation between the fast and slow waveforms; (c) linear particle motion; (d) a unique, well-defined error surface. For *SK(K)S* splitting analysis, we preformed three methods with the SplitLab, and chose only those results with the fast direction difference <25° for all the three pairs between RC, SC and EV. Figures 2 and 3 shows representative examples of local *S* and *SKS* wave splitting measurements. All splitting measurements are presented in Figures S1, S2, and S3 in Supporting Information S1. Figure S4 in Supporting Information S1 shows stations with no apparent splitting (i.e., a null measurement). This

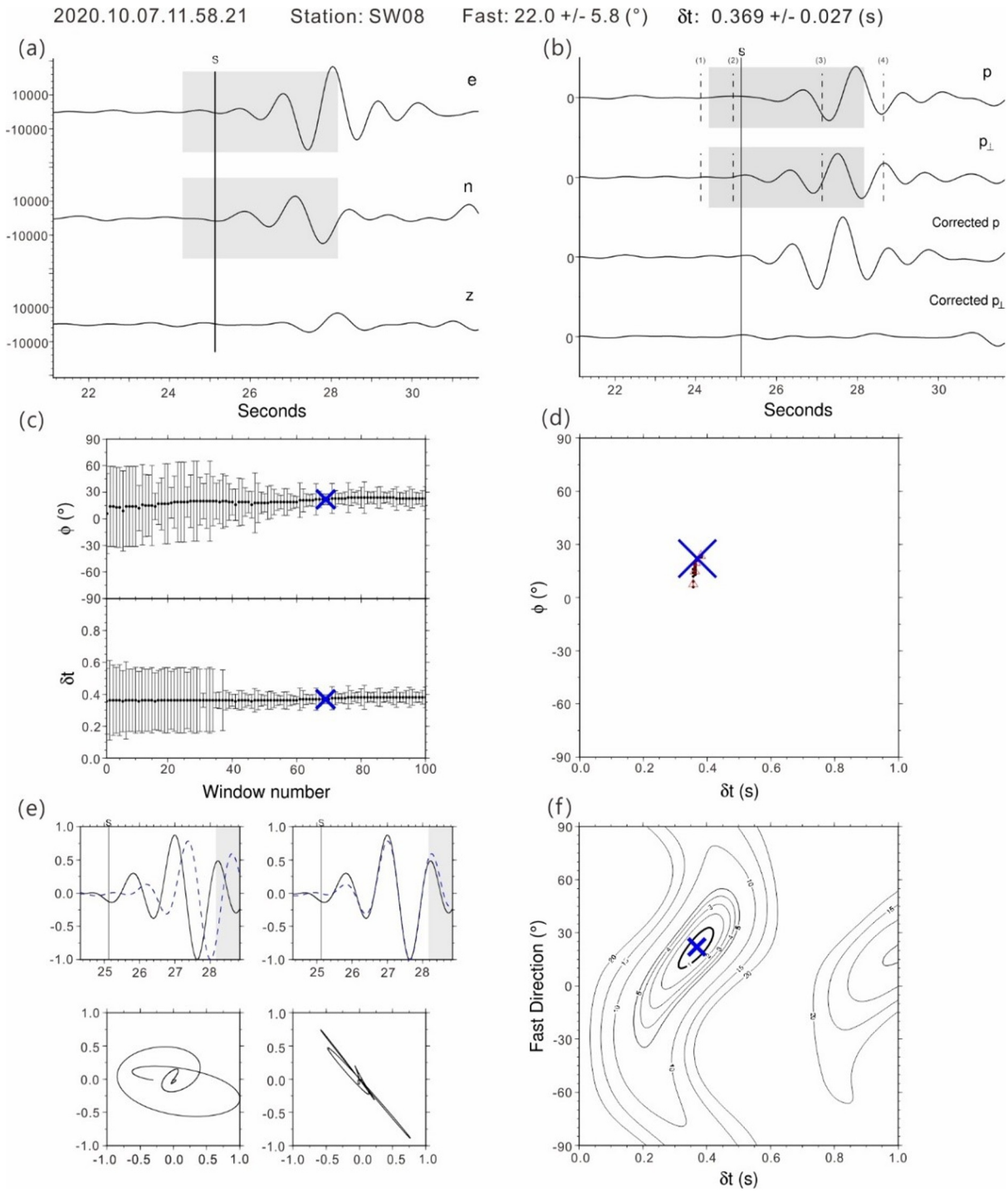

Figure 2. A typical example of splitting measurements from local S phases using the Multiple Frequency Automatic Splitting Technique (MFAST) software package. Top: event origin time, station name and anisotropic parameters derived in this study. From middle left to bottom right: three components of local S waveforms filter at 0.1–1 Hz, the components of incoming polarization direction and its perpendicular for S splitting before and after the correction, measurements of φ and δt obtained from 100 different analysis windows plotted against window number, cluster analysis with a blue cross marking the optimum cluster, with the lowest variance σ2, fast and slow shear waveforms (top; the area with gray-shaded background is outside the chosen measurement window) and particle motion (bottom) before (left) and after (right) the shearwave splitting correction, and grid search map for optimal φ and δt (blue cross) along with 95% confidence region.

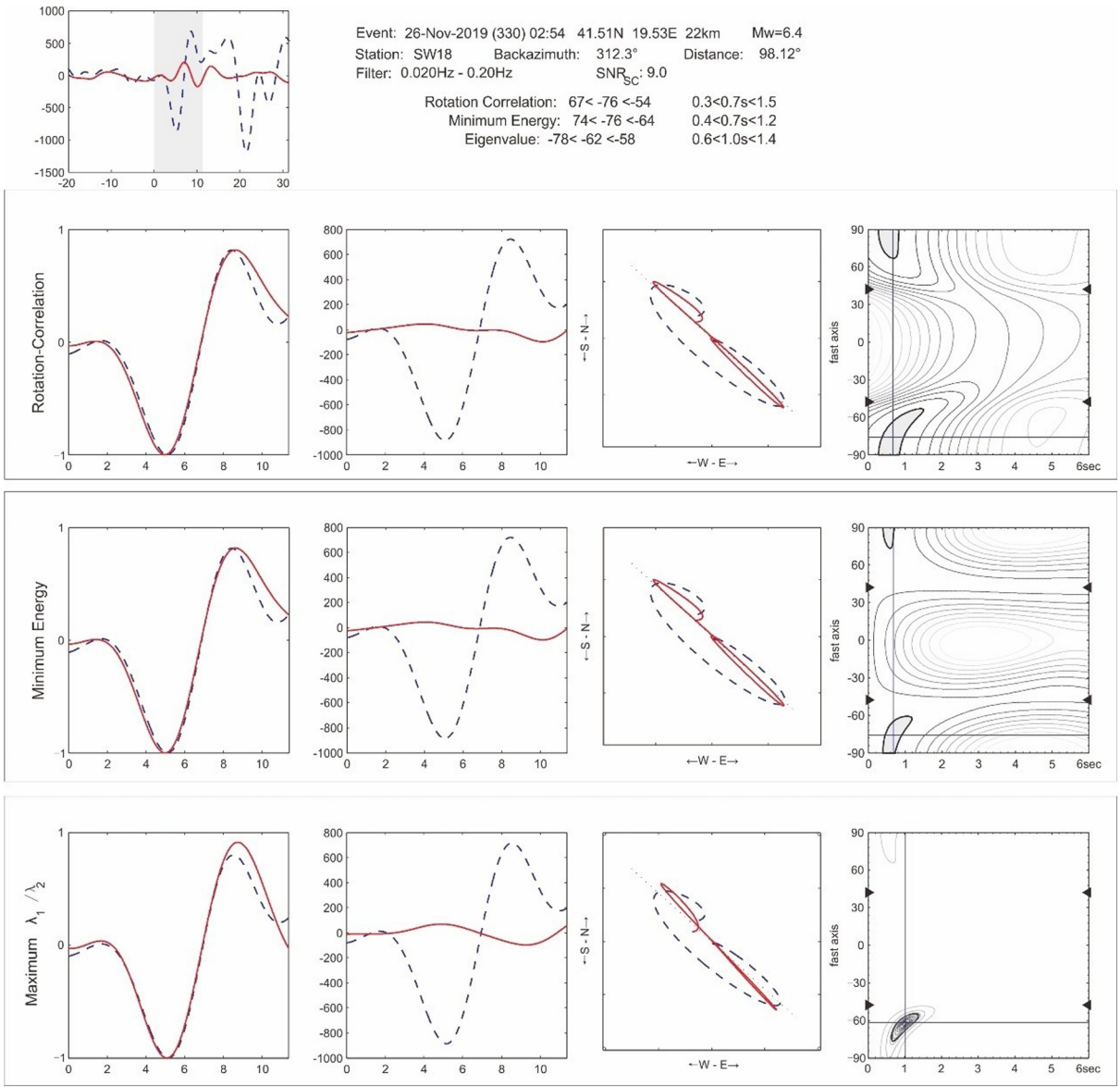

Figure 3. A good example of *SKS*-phase splitting measurements using the SplitLab software package used in the final analysis. An extended section of radial (dashed) and transverse (solid) components before anisotropic correction is shown at the top, together with event information and values of splitting measurements. Results are obtained with the rotation correlation method (RC, second row), the minimum energy method (SC, third row) and the eigenvalue method (bottom row). For each row from left to right: fast (dashed) and slow (solid) shear waveforms after the splitting correction, radial (dashed) and transverse (solid) components after correction, particle motion before (dashed) and after (solid) correction, and results of grid search for optimal φ and δt (cross). The thick contour marks the 95% confidence interval.

can be explained by the shear wave traveling through an isotropic medium or the initial polarization (*SKS* back-azimuth) coinciding with the fast or slow polarization directions (Wüstefeld et al., 2008).

Following our selecting criteria, the analysis yielded (a) five good splitting measurements and three nulls for *SKS* waves, (b) three measurements for teleseismic *S*, and (c) 18 local *S* splitting measurements. The event-station pairs for teleseismic *S* and *SKS* waves involve nine teleseismic events recorded at eight stations. Those for local *S* waves are based on 14 local events recorded at three stations (Tables 2–4, and Figure 4). To compare with the results from the MFAST, the EV results from the SplitLab are chosen to show in Figure 6. Measurement errors from the MFAST represent one standard deviation (Marson-Pidgeon & Savage, 2004), while those from the EV of the SplitLab are set as boundaries of the minimum and maximum range of the 2-sigma confidence region (Wüstefeld et al., 2008) (Table 3). The F test is used to calculate the 95% confidence interval for the optimum

Table 2
Local S Wave Splitting Results

	Event information					Splitting results			
Station	Date	Lon (°)	Lat (°)	Dep (km)	Mag	δt (s)	$\sigma_{\delta t}$ (s)	φ (°)	σ_{φ} (°)
SW08	2019-12-10	0.13	121.70	179.5	4.1	0.30	0.02	0	7
SW08	2020-01-01	0.19	121.56	141.3	4.1	0.32	0.01	−14	3.5
SW08	2020-01-20	0.33	122.35	172.5	4.2	0.17	0.02	14	6
SW08	2020-05-18	0.19	121.01	158.5	4.4	0.36	0.01	−80	3.5
SW08	2020-07-24	4.11	122.74	583.2	5	0.39	0.07	−66	25.75
SW08	2020-09-04	3.49	122.15	596.5	4.4	0.28	0.03	−70	11.5
SW08	2020-10-07	0.58	121.49	99.1	4.3	0.37	0.03	22	5.75
SW08	2020-10-26	0.58	121.54	90.0	5.1	0.41	0.01	34	3.5
SW17	2019-12-10	0.13	121.70	179.5	4.1	0.39	0.00	61	1
SW17	2020-03-30	0.67	121.59	99.0	4.3	0.39	0.02	16	3.25
SW17	2020-05-18	0.19	121.01	158.5	4.4	0.41	0.05	−15	5.25
SW17	2020-07-11	0.21	120.79	109.3	4.8	0.51	0.06	−43	8
SW17	2020-10-07	0.58	121.49	99.1	4.3	0.26	0.02	−3	8.5
TOLI	2009–03.30	3.80	122.31	604	4.1	0.93	0.05	−86	6.75
TOLI	2009-07-03	4.69	123.05	582	4	0.36	0.03	−43	4.5
TOLI	2009-10-10	3.86	122.45	601	5.1	0.88	0.06	−84	5.25
TOLI	2015-04-27	3.63	123.07	500	4.3	0.39	0.02	−42	4.75
TOLI	2016-05-20	2.46	120.99	673.1	4.8	0.34	0.11	−41	16

Note. $\sigma_{\delta t}$ and σ_{φ} are the uncertainties of δt and φ by using MFAST, respectively.

values for the two shear wave splitting parameters (φ and δt), under the assumption that the minimum of the grid-search surface (e.g., E_t (φ, δt) or λ_2 (φ, δt)) is a χ^2 variable with *n* degrees of freedom. The inequality contains the eigenvalue, the inverse of the statistical F distribution and the number of degrees of freedom of the signal that is processed (e.g., Silver & Chan, 1991; Walsh et al., 2013).

Table 3
All Teleseismic S and SKS-Phase Splitting Results From the EV Method

	Event information					Splitting results		
Station	Date	Lon (°)	Lat (°)	Dep (km)	Mag	δt (s)	φ (°)	Phase
SW01	2020/9/26	31.76	−48.03	10	6.1	−37 < −20 < −7	1.0 < 1.3 < 1.6	SKS
SW06	2021/2/24	−22.29	63.95	10	5.6	27 < 43 < 62	1.6 < 1.8 < 2.1	SKS
SW08	2020/2/14	−142.29	−56.66	10	5.6	84 < −75 < −64	1.8 < 2.9 < 4.3	SKS
SW08	2020/10/6	−178.48	−18.01	634	6	−80.0 ± 1.8	1.7 ± 0.03	S
SW17	2019/12/25	−115.84	−25.22	10	6.1	46 < 69 < −76	1.3 < 2.2 < 3.4	SKS
SW18	2019/11/26	19.53	41.51	22	6.4	−64 ± 1.2	1.0 ± 0.04	SKS
SW20	2020/6/19	−178.92	−17.45	535	5.6	9.0 ± 19.8	0.6 ± 1.02	S
SW20	2020/10/6	−178.48	−18.01	634	6	28.0 ± 16.5	1.6 ± 0.45	S

Note. Splitting results from the EV method (MFAST for teleseismic S-wave splitting, SplitLab for SKS wave splitting) are shown in this Table. Measurement errors from the MFAST represent one standard deviation (Marson-Pidgeon & Savage, 2004), while those from the EV of the SplitLab are set as boundaries of the minimum and maximum range of the 2-sigma confidence region (Wüstefeld et al., 2008). All results are provided in Figures S2 and S3 in Supporting Information S1.

Table 4
Null Measurements From SKS Waves

Station	Event information							Phase
	Date	Lon (°)	Lat (°)	Dep (km)	Mag	Dist (°)	Baz (°)	
SW05	2020/1/6	0.23	−16.99	10	5.6	137.03	268.91	SKS
SW07	2021/1/11	−58.05	−9.84	10	5.5	109.65	205.77	SKS
SW17	2020/1/6	0.23	−16.99	10	5.6	138.64	270.19	SKS

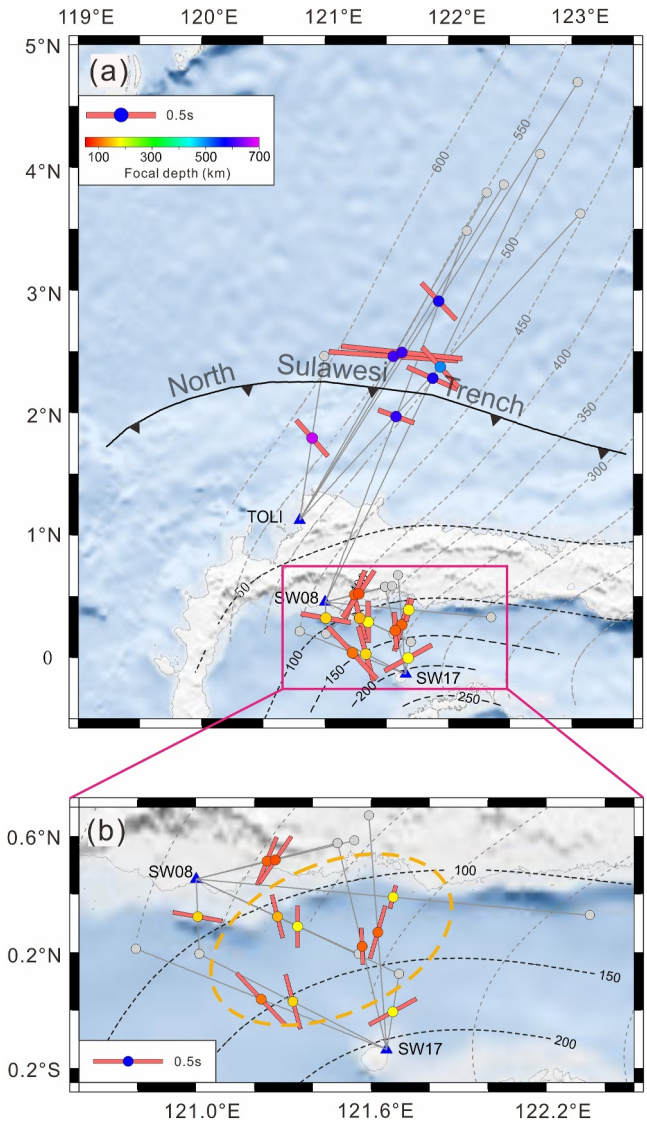

Figure 4. (a) All the local S-wave splitting measurements, and (b) a zoom-in of the results shown in the magenta rectangle in (a). Splitting measurements are plotted at the center point (circles colored according to the focal depth) between the events (gray circles) and stations (blue triangles). The orientation of each bar is parallel to the measured fast polarization of anisotropy and the length is scaled according to delay time. The depth contours of the Celebes Sea (black) and Sangihe (gray) plate interface (in km) are from Hayes et al. (2018). The orange dotted ellipse encloses the results with fast directions normal to the strike of the CSS.

3. Shear Wave Splitting Results

3.1. Local *S*-Phase Splitting Measurements

For the local *S*-phase splitting, our analyses yielded 18 reliable results, presented in Table 2 and Figure 4, 11 of which are magnified in Figure 4b for clarity. Overall, the delay times range from 0.16 to 0.93 s. In the north (between 1.5° and 3°N) the fast polarizations are spatially parallel confined to the North Sulawesi trench (Figure 4a), but normal to the Sangihe trench at the regional scale. In the south normal to oblique to the North Sulawesi trench (Figure 4b) directions are observed. Figure 5 shows the distribution of δt with respect to source depth and latitude of the center point between the events and stations events used in the central ellipse in Figure 4b. We observe no clear correlation between δt and source depth but a variation with the latitude of the center points.

3.2. Teleseismic *S* and *SKS*-Phase Splitting

The teleseismic *S* and *SKS* phase splitting parameters (φ and δt) and null results are presented in Figure 6 and Tables 3 and 4. All the null measurements appear to be related to events coming from back-azimuths that are either ∼parallel or ∼perpendicular to the fast directions of the stations. Station SW17, which lies near Una-Una volcano, yields one reliable *SKS* splitting measurement with a φ of 69.3° and δt of 2.2 s and one null result.

Of two temporary stations (SW08 and SW18) located on the northern arm of Sulawesi, SW18 only has one splitting result, with φ of −61.7° and δt of 1.0 s, whereas SW08 has two splitting results and one null result. The average splitting parameter values at SW08 are φ = −77.6° and δt = 2.3 s. In this study, only SW08 has two non-null results. The average φ and δt are calculated based on the method of averaging directional data described by Kubo and Hiramatsu (1998). Fast directions of anisotropy at these two stations are all oblique to the North Sulawesi trench (or normal to the Sangihe trench).

Five stations (SW01, SW05, SW06, SW07, and SW20) are adjacent to the PKF in the southern part of our study area. Four splitting results (one for SW01, one for SW06, and two for SW20) and two null results for SW05 and SW07 are obtained. However, the distribution of the φ measurements is diverse: ∼fault-parallel (N–S) at SW01, fault-oblique (NE–SW or NNE–SSW) at SW06 and SW20, and a wide range of δt between 0.6 and 1.8 s are also obtained.

4. Discussion

4.1. Sources of Observed Seismic Anisotropy

In most regions of the upper mantle, seismic anisotropy is mainly caused by the crystallographic preferred orientation (CPO) of mantle minerals, that is,

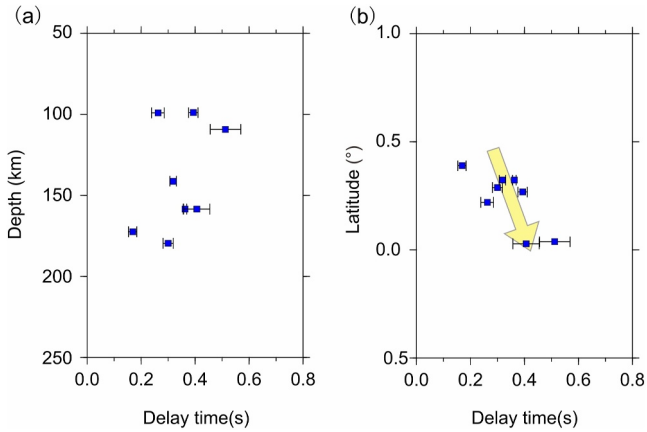

Figure 5. (a) Depth versus δt values (blue squares with black bars denote the delay times and their errors) at stations SW08 and SW17 shown in the orange dotted ellipse in Figure 4b; (b) Latitude of the center point between the events and stations versus δt values for the same events in (a). The yellow arrow indicates the trend of δt values with respect to latitude.

primarily olivine, induced by mantle flow due to slab subduction (Wolfe & Silver, 1998). The classical model for the mantle flow field in subduction zones is two-dimensional and is associated with two dominant regions. One is the mantle wedge, characterized by viscous coupling between the downgoing slab and the mantle above the subducting slab, resulting in corner flow. The other is the mantle below the slab, where entrained flow occurs (Hall et al., 2000; Ribe, 1989). In general, plate motion-parallel fast directions are predicted in the mantle wedge by this model (Long & Silver, 2008), which, however, deviates from complicated observations from most subduction zones: for example, trench-parallel beneath Tonga (Smith et al., 2001), Costa Rica (Hoernle et al., 2008); both trench-parallel and -normal beneath Ryukyu (Long & van der Hilst, 2006) and Japan (Long & van der Hilst, 2005); and trench-oblique beneath the north of the Philippine (Wang & He, 2020). In the subslab mantle, trench-parallel mantle flow might exist below the subducting slab in the case of slab rollback (Long & Silver, 2008). Long (2013) suggested that mantle flow in the mantle wedge and subslab mantle may be entangled by many factors, for example, slab age, slab morphology, and surrounding flow field, can affect the overall flow pattern. Therefore, a single model cannot adequately explain all observations across different regions, especially in our study area, mantle deformation likely results from the combined effects of multiple subduction zones.

In most subduction regions, mantle deformation has been inferred by measuring the splitting of shear waves and carefully analyzing the potential sources of seismic anisotropy with different phases. The core-refracted *SKS*

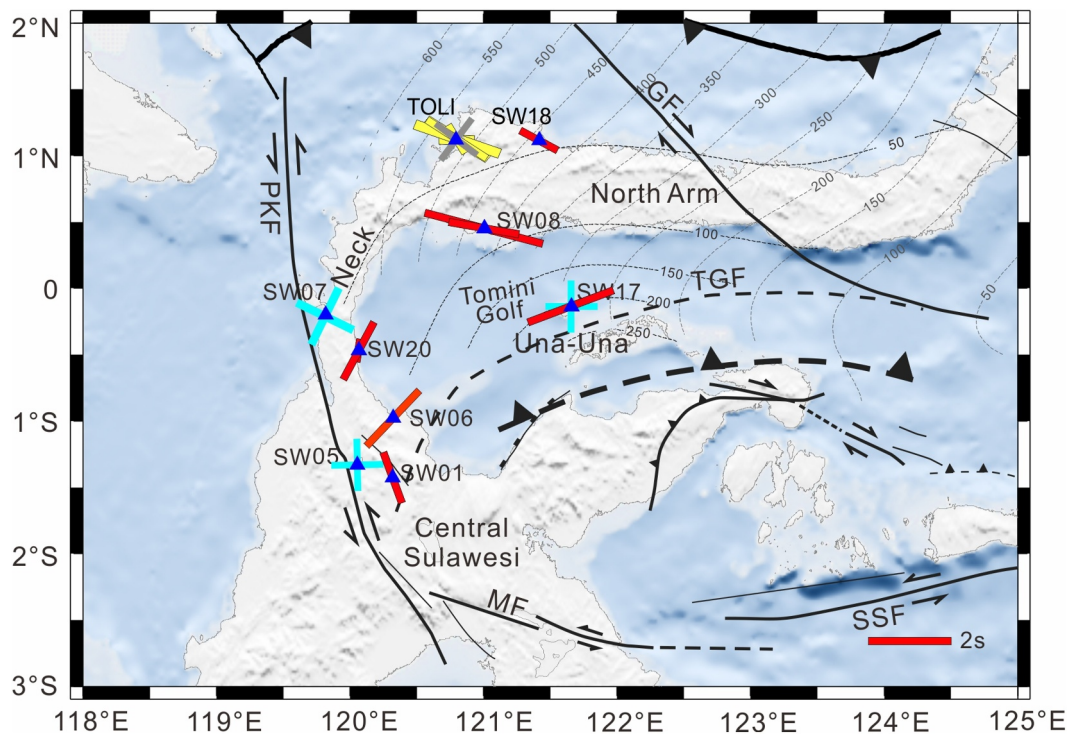

Figure 6. The results of all teleseismic *S* and *SK(K)S*-wave splitting (red bars), and null (light blue bars) measurements obtained from this study, along with previous results at TOLI from *SKS*-phase splitting by Di Leo et al. (2012a) and Cao et al. (2021; splitting and null measurements shown as yellow and gray bars, respectively). All results are plotted at the location of stations (blue triangles). The orientation of each red bar indicates the corresponding fast polarization orientation and its length is proportional to the delay time. The contours of plate interface depths (in km) are from Hayes et al. (2018). The thick dotted line shows the inferred position of the trench associated with the fully submerged Sula slab (Hall & Spakman, 2015). PKF: Palu-Koro fault; MF: Matano fault.

phases sample integrated anisotropy along the path from the core-mantle boundary to the station, covering the subducting slab, overriding crust, mantle wedge and subslab mantle. Local *S* phases originating from slab earthquakes mainly sample anisotropy in the overriding lithosphere and mantle wedge. Teleseismic *S* from deep earthquakes can be carefully used, assuming that the source-side seismic anisotropy in the transition zone and lower mantle is weak and neglected (Long & van der Hilst, 2005; Lynner & Long, 2014; Marson-Pidgeon & Savage, 1997). In addition, source-side *S* phases originating from slab earthquakes are sensitive to anisotropy in the sub-slab mantle after the signal from anisotropy beneath the receiver is accounted for (Lynner & Long, 2013, 2014; Roy et al., 2017).

A regional scale 3-D *P* wave anisotropic tomography study found Sangihe trench-normal anisotropy beneath the Celebes Sea at 150 km depth (Huang et al., 2015), in contrast to trench-oblique anisotropy in Hua et al. (2022)'s results. Beneath the North Sulawesi, the resolution of *P* azimuth anisotropy may not be good enough to resolve the lateral variation of mantle deformation associated with the interaction of multiple subducted slabs (Hua et al., 2022; Huang et al., 2015). To better constrain sources of anisotropy in complex subduction systems, a key method is analyzing shear wave splitting in various waveforms originating from different depths.

The station's location, slab morphology, geometry of the trench, and hypocentral location of the earthquake are all important in determining the contribution of different domains. It has been suggested that the average crustal contribution is on the order of 0.1 s globally, and the contribution from the lower mantle and transition zone is less than 0.2 s (Silver, 1996). The typical values of δt from *SKS* splitting in this study are more than 1 s, indicating that anisotropy primarily comes from the upper mantle beneath the Moho (Silver, 1996). More specifically, the average value of δt from *SKS* is 1.6 s, and more than 88% of values are larger than 1 s. A thin crust along the western part of the north arm of Sulawesi with about 20–25 km thickness has been proposed based on the receiver function analysis (Fauzi et al., 2021; Linang, 2023). Previous investigations in subduction zone settings support our inference that the dominant contributor of seismic anisotropy in the upper mantle is mantle wedge flow (e.g., Cao et al., 2021; León Soto & Valenzuela, 2013; Long & Wirth, 2013; Wang & He, 2020), though the upper plate crust and subducting slab may also contribute. However, it is likely to insignificant in comparison, as discussed above, unless the upper plate is of cratonic origin (Yuan et al., 2011), which is not the case here. Although the upper mantle is likely to be the primary source of anisotropy, careful analysis must be taken to infer anisotropic fabrics in different domains in such a complex tectonic setting caused by slab-slab interaction. For this purpose, we comprehensively compare anisotropic parameters from local *S* and teleseismic *S/SKS/SKKS* waves in this study and previous source-side *S* splitting (Di Leo et al., 2012b).

4.2. Corner Flow in the Sangihe Subduction Zone

Generally, corner flow within the mantle wedge, developed by viscous coupling between the down-going slab and the overlying mantle, produces trench-normal fast directions in back-arc regions (Long & Wirth, 2013). Eight deep events from our local *S*-phase splitting measurements affiliated with the SHS show a ubiquitously coherent fast direction pattern normal to the Sangihe trench (Figure 4a). This can be readily attributed to corner flow within the mantle wedge above the westward subducting SHS (Long & Wirth, 2013). Based on intraslab seismicity (Hutchings & Mooney, 2021) and tomographic images (Hall & Spakman, 2015; Wehner et al., 2022; Zenonos et al., 2019), the SHS has reached the mantle transition zone, resulting in a large volume of mantle wedge above. The development of a large mantle wedge is suggested by numerical modeling (e.g., Dal Zilio et al., 2017). Our local *S* splitting results at SW08 and SW18 reconcile with the fast directions of anisotropy from teleseismic *S* and *SKS* at TOLI and source-side *S* to the east of these two stations from previous studies (Cao et al., 2021; Di Leo et al., 2012a, 2012b). They are mainly normal to the strike of the westward subducting Sangihe slab. The large δt of >2.0 s was observed at SW08, possibly due to joint contributions from both mantle wedge flows with similar flow patterns above the SHS and the CSS. In addition, the average value of δt from source-side *S* phases (0.74 s; Di Leo et al., 2012b) is much larger than the average δt (0.35 s) from local *S* of events shallower than 200 km. In summary, the upper-mantle flow pattern beneath the CSS within the Sangihe subduction system is dominated by the trench-normal mantle wedge flow above the SHS (Arrow #1 in Figure 7).

4.3. Corner Flow in the North Sulawesi Subduction Zone

Although the North Sulawesi subduction zone (NSSZ) is smaller compared to the Sangihe subduction zone, the trench-normal fast polarization of anisotropy from the *SKS* measurement is also dominant (Figure 4). The pattern

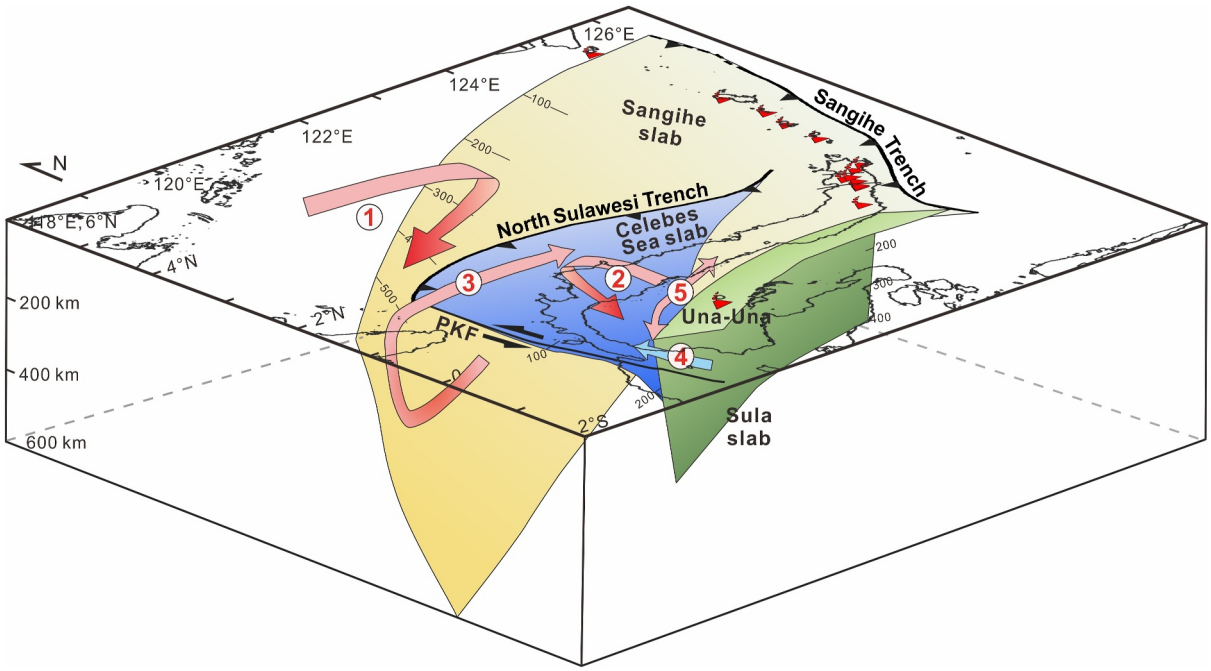

Figure 7. Schematic cartoon illustrating the tectonic setting of multiple subduction zones (based on a model shown in Hall & Spakman, 2015) and interpreted mantle flows (red arrows) and lithospheric-asthenospheric deformation (blue arrow) in the study region. Arrows #1 and #2 indicate corner flows induced by the subduction of the larger Sangihe and smaller Celebes Sea slabs, respectively. Arrow #3 denotes a similar corner flow to #1 related to subduction of the SHS, but this branch flows into the mantle wedge above the subducting CSS. Arrow #4 shows combined anisotropy from both the lithospheric scale PKF and possible N-S asthenospheric flow underneath. Arrow #5 represents flow associated with the submerged Sula slab. The names of slabs in and around North Sulawesi are adopted from Hall and Spakman (2015).

of fast polarization orientations observed in the mantle wedge of the NSSZ (Figure 4b) (the 11 local *S*-wave splits from SW08 and SW17) can be divided into three sub-regions (north, central and south; Figure 4b): the north includes three measurements mainly corresponding to the onshore part of the North Sula block, the central consists of seven measurements (as shown in the orange ellipse in Figure 4b, the offshore region between the island and the Una-Una volcano), and the south has only one measurement very close to the Una-Una Volcano.

When excluding the four measurements in the north and south, the seven measurements in the center do not exhibit either trench-normal or trench oblique (relative to the North Sulawesi trench) orientation; instead, they show fast directions normal to the strike of the CSS (the contours shown in Figure 4). The fast axis orientations of anisotropy could be attributed to the crust and/or deformation of the mantle wedge. The maximum compressive stress (S_{Hmax}) direction in the overlying crust obtained from moment tensor solutions is found to be normal to the trench (Greenfield et al., 2021), which for the case of EDA (Extensive Dilatancy Anisotropy), where anisotropy is controlled by fluid filled cracks aligned to SHmax (e.g., Crampin, 1994), would result in fast axis orientations of anisotropy to also be trench-normal (e.g., Matharu et al., 2014). However, axis orientations of anisotropy in the forearc region are not perpendicular to the North Sulawesi trench. Close inspection shows that from east to west, the fast axis gradually rotates and closely follows the arcuate depth contours of the CSS, especially in the west, which indicates that the fast axis is normal to the previous trench strike, which is caused by clockwise retreat of the Sulawesi trench over the past 5 Myrs. Such a slab strike-dependent signature is predicted by many numerical models (e.g., Honda & Yoshida, 2005; Wada, 2021), which suggests that the mantle wedge inflow patterns above the downgoing slab are mainly influenced by the slab, with flow direction related to arcuate geometry of the subducted CSS based on the depth contours of the CSS interface (Figure 4). As shown in the central region where SHS influence is minimal, the induced mantle flow pattern with fast directions normal to the depth contours of the CSS interface is clearly influenced by the subduction of the CSS (Arrow #2 in Figure 7).

Variation from trench-normal to slab-strike-normal anisotropy is also observed at other subduction settings along the Pacific plate boundary (e.g., León Soto & Valenzuela, 2013; Long & Wirth, 2013; Wang & He, 2020). It demonstrates that the most dominant flow type within a subduction zone is generally the corner flow, which

depends on the downgoing direction of the dipping slab. Its influence gradually fades away with distance, particularly at the slab edges as we will demonstrate by the remaining four measurements in the north and south regions of the mantle wedge of the NSSZ, where slab-slab interactions influence the results.

Delay times from seven local *S*-wave splitting measurements in the central region (Figure 4b) range from 0.17 to 0.51 s, with an average value of 0.34 s, similar to the average results obtained at several other subduction zones around the Pacific (Long & Wirth, 2013). In the center of the corner flow of the NSSZ, the δt values show a decrease in strength of anisotropy from south to north, which can be corroborated by numerical modeling (e.g., Dal Zilio et al., 2017; Dong et al., 2022; Gérault et al., 2012). Given that the global average splitting time of continental crust is on the order of 0.1 s (Silver, 1996), we suggest that mantle wedge flow is the main source of local shear-wave splitting at intermediate depth, with potentially a certain degree of anisotropy also coming from the subducting slab and overriding lithosphere. Overall, we argue for the critical role of mantle wedge flow in explaining local *S*-wave splitting, as has been well established by other subduction zone studies (e.g., Cao et al., 2021; León Soto & Valenzuela, 2013; Long & Wirth, 2013; Wang & He, 2020).

Multi-layered anisotropy is suggested to explain some complex anisotropy patterns in a subduction system (Long & Silver, 2009; Silver & Chan, 1991). In a specific case like SW08 (Figure 6), as mentioned above, a two-layer model with similar fast directions is seemingly required largely due to the presence of a double orthogonal subduction system involving the horizontal overlap of two slabs. The raypaths from medium (<200 km) and deep events (>500 km) to SW08 come from northeast and east-to-south, respectively, which cannot constrain the subslab mantle flow. A previous seismic anisotropy study has suggested that the *SKS*-wave splitting measurements at TOLI may be explained by most contributions from mantle wedge flow in the Sangihe subduction zone, with a minor influence of the corner flow in the Celebes mantle wedge (Cao et al., 2021). Still, for each subduction zone, the mantle wedge flow is the leading cause of upper-mantle seismic anisotropy. The nature of the slab-slab interactions illuminated in this study will be discussed further in the following subsection.

4.4. Upper Mantle Deformation Related to Dynamic Interaction Between Two Subduction Zones

Numerical experiments suggest that two (or more) adjacent slabs interact via forces transmitted through the lithosphere and the underlying mantle (e.g., Király et al., 2016, 2018b, 2021). Consequently, slab-slab interaction can mutually influence the subduction evolution, mantle flow and stress propagation through the mantle (Király et al., 2016). How one downgoing slab can dynamically act on another downgoing slab in the upper mantle is not well constrained by observations, especially in terms of the complexity of corner flows induced by adjacent subducting slabs. In our study area, the North Sulawesi subduction system is located at the southwest margin of the Sangihe subduction system, and the subduction directions of the two plates are nearly perpendicular. To the south of the North Sulawesi subduction system, the SLS has subducted to more than 600 km depth. The slab-slab interaction between the CSS and the SHS, and between the CSS and the SLS affect the upper mantle deformation, which could be investigated through seismic anisotropy observations.

The southward subducting CSS alone does not explain our three local *S*-wave splitting results. The fast polarization orientations of the three northernmost measurements are not normal to the strike of the slab (Figure 4b). Therefore, we attribute the largely trench-oblique fast polarizations to flow in the mantle wedge above the CSS, which was deflected by the eastward corner flow of the subducting SHS (Arrow 3 in Figure 7). This is plausible because the two downgoing slabs overlap in space, evidenced by the region's seismicity and tomographic images (Figure 1; Hall & Spakman, 2015; Hutchings & Mooney, 2021). However, it is important to understand why the signature of the interactions can only be detected in these three measurements. This may be explained by the corner flow associated with the SHS diminishing eastward as it becomes hindered by southward flow above the CSS. In addition, numerical modeling (e.g., Dal Zilio et al., 2017; Dong et al., 2022; Gérault et al., 2012) also suggests that the return flow above a slab decreases toward the trench, which may help produce a flow interaction that attenuates from west to east, as observed here.

From the center of the NSSZ to the south, the fast polarization orientation of anisotropy changes from normal to the strike of the subducting CSS to parallel to its strike. The southernmost measurement (SW17) has an ENE–WSW-trending fast polarization direction of anisotropy that cannot be explained by the southward subduction of the CSS alone. We attribute this observation to the interaction between the CSS and the SLS. Based on the distribution of seismicity and recent tomographic images (Hall & Spakman, 2015; Hutchings & Mooney, 2021), the subducted SLS resides above the 660 km discontinuity. Considering the extinct north-dipping slab (the fully

submerged SLS), the fast polarization orientation of anisotropy observed at station SW17, largely parallel to the strike of the SLS, may suggest that the corner flow associated with the subduction of the CSS was blocked by the SLS (Arrow #5 in Figure 7). Based on the observations above, we infer that the inward subduction of two neighboring slabs could affect the mantle flow between them only when the two slabs are either close enough that one slab blocks the mantle flow induced by the other slab or partly overlapping.

4.5. Lithospheric Deformation Along the Strike-Slip Palu-Koro Fault

Another goal of this study is to understand to what extent the PKF accommodates regional crustal and upper-mantle deformation. In the western Sula block, the N–S-trending fast polarization of anisotropy from *SKS*-splitting, subparallel to the PKF, is observed at station SW01, which is consistent with the sinistral strike-slip motion between the North Sula block and the Makassar block (Socquet et al., 2006). The delay time of 1.3 s observed at SW01 is larger than the global average value of ∼1.0 s typically attributed to mantle lithosphere deformation (Silver, 1996). It is, however, smaller than measurements from the Alpine fault system in New Zealand, where similar strike-parallel anisotropy measurements have an average value of 2 s (Savage et al., 2004; Zietlow et al., 2014). Savage et al. (2004) attributed this large average splitting time to strong coupling between the surface and the deeper mantle.

Global positioning system (GPS) measurements indicate that the motion of the western segment of the North Arm of Sulawesi relative to the Sunda plate is faster than the eastern segment (Socquet et al., 2006; Walpersdorf et al., 1998). The PKF, located on the western boundary of the NSSZ, accommodates the rotation of the North Arm and the trench retreat, with the GPS velocities east of the PKF being nearly twice the GPS velocities to the west (Socquet et al., 2006). Tomographic models (Hall & Spakman, 2015; Wehner et al., 2022) indicate a large lithospheric thickness variation across the PKF, with much thinner lithosphere in the east. This is supported by the fact that lithosphere of Gondwana origin flanks the PKF on the west, whereas the east comprises fragmented microcontinent from the Sula Spur (Hall & Sevastjanova, 2012; Song et al., 2022). The PKF is therefore most likely a lithospheric-scale boundary, and the thinner lithosphere in the east with higher GPS velocity would accommodate large N-S lithospheric deformation, contributing to the large splitting measurement at station SW01 (Arrow 4 in Figure 7).

An anisotropic lithosphere of ∼200 km thickness with 2% anisotropy may result in a splitting time of 1 s (Silver, 1996). The lithospheric thickness beneath the PKF is significantly less than 200 km (Figure 11 in Wehner et al., 2022), thus the 1.3 s delay time at station SW01 may require substantial lithosphere and asthenosphere coupling. A N-S directed mantle flow beneath station SW01 may also be required to contribute to the 1.3 s fault-parallel anisotropy. Fault-oblique (∼45°) fast polarization orientations of anisotropy observed at SW06 and SW20, in line with the back-azimuth of the null result at SW07, appear to be parallel to the strike of the Celebes Sea slab. At the western edge of the NSSZ, downgoing CSS induced corner flow might not be vigorous enough to influence this observation. Therefore, we first attribute these observations to edge effects because they are close to the western edge of the subducting CSS. Additionally, the fast directions oblique to the strike of the fault could also be attributed to the N–S-trending mantle flow, inferred to be present beneath station SW01, which is deflected by thicker lithosphere on the west side of the PKF (e.g., Figure 11 in Wehner et al., 2022), and channeled in a N-S direction beneath the fault system.

In the immediate vicinity of the fault, however, the nulls at SW05 and SW07 may be due to a combined effect of the complex but localized deformation systems underneath the fault zone: that is, the north-south oriented fault system; asymmetric lithospheric deformation away from the fault (see above for stations SW01); and the eastward thinning (e.g., Wehner et al., 2022) of the lithosphere across the fault. These systems might lead to cancellation of their corresponding anisotropic signals. Alternatively, it may be due to back-azimuths parallel or perpendicular to the initial polarization directions. The discussion above is based on our analysis of the splitting results and the known geometry of the subducting slabs in the region. A more quantitative analysis would necessitate numerical modeling of mantle flow.

5. Conclusions

In this study, we attempt to understand the dynamic interactions of mantle wedge flow in the Sangihe, North Sulawesi subduction zones and around the edge of the Celebes Sea slab affected by the Palu-Koro strike-slip fault. To achieve this, we employ shear-wave splitting analysis of local *S* and teleseismic core-refracted phases to

characterize the regional upper-mantle anisotropy. The inferred upper-mantle seismic anisotropy corresponds well with the regional deformation in North Sulawesi, where the adjacent slab-slab interaction more strongly influences the mantle flow pattern. The regional microtectonic boundary, the Palu-Koro fault, influences the measurement considerably by confining the lithosphere-scale deformation within the North Sula block. This suggests that the Palu-Koro fault is a microtectonic boundary that accommodates the differential motion between the North Sulawesi block and Makassar block.

We also suggest that seismic anisotropy patterns in this region can be mainly attributed to deformation in the mantle wedge of the Sangihe and North Sulawesi subduction zones and along the Palu-Koro fault, particularly in consideration of the Celebes Sea slab geometry and fault movement directions. Furthermore, consistent with the findings of numerous structural geology studies that the Palu-Koro fault represents the suture boundary between two drifting microblocks, we here demonstrate that it is possible to identify a concealed tectonic boundary using shear-wave splitting analysis.

Data Availability Statement

All raw waveforms in the three components used in this study can be provided by Cao et al. (2024), which will be openly accessible at the public repository of Zenodo via https://zenodo.org/record/7758460#.ZBpqRxRBxdg. Two shear waves splitting analysis software packages used in this study — SplitLab (Wüstefeld et al., 2008) and MFAST (Teanby et al., 2004) can be obtained via http://github.com/IPGP/splitlab and http://mfast-package.geo.vuw.ac.nz/, respectively. Some figures were prepared using the Generic Mapping Tools (Wessel & Smith, 1991).

Acknowledgments
The authors acknowledge support from the Strategic Priority Research Program of the Chinese Academy of Sciences (Grant XDB42020103) and the National Scientific Foundation of China (Grants 42076068 and 91955210). The seismic deployment in Sulawesi was funded by a British Council Newton Grant (G107511) and the Global Challenges Research Fund Grant (G102642) to CL, NR, and SW. This work was also supported by the NSFC Major Research Plan on West-Pacific Earth System Multi-spheric Interactions (91858212 and 91958212) and Isaac Newton Trust of Cambridge.

References

Amaru, M. L. (2007). *Global travel time tomography with 3-D reference models (PhD thesis)*. Utrecht University.

Booth, D. C., & Crampin, S. (1985). Shear-wave polarization on a curved wavefront at an isotropic free surface. *Geophysical Journal of the Royal Astronomical Society*, *83*(1), 31–45. https://doi.org/10.1111/j.1365-246x.1985.tb05154.x

Bowman, J. R., & Ando, M. (1987). Shear-wave splitting in the upper-mantle wedge above the Tonga subduction zone. *Geophysical Journal of the Royal Astronomical Society*, *88*(1), 25–41. https://doi.org/10.1111/j.1365-246x.1987.tb01367.x

Cao, L. M., He, X. B., Zhao, L., Lü, C. C., Hao, T. Y., Zhao, M. H., & Qiu, X. L. (2021). Mantle flow patterns beneath the junction of multiple subduction systems between the Pacific and Tethys domains, SE Asia: Constraints from SKS-wave splitting measurements. *Geochemistry, Geophysics, Geosystems*, *22*(9), e2021GC009700. https://doi.org/10.1029/2021GC009700

Cao, L. M., Lü, C. C., He, X. B., Hao, T. Y., Widiyantoro, S., Supendi, P., et al. (2024). Mantle flow induced by the interplay of downgoing slabs revealed by seismic anisotropy beneath the Sula Block in eastern Indonesia [Dataset]. *Zenodo*. https://zenodo.org/record/7758460#.ZBpqRxRBxdg

Cardwell, R. K., Isacks, B. L., & Karig, D. E. (1980). The spatial distribution of earthquakes, focal mechanism solutions, and plate boundaries in the Philippine and Northeastern Indonesian Islands. In D. E. Hayes (Ed.), *The tectonic and geologic evolution of southeast Asian seas and islands*, *Geophysical Monograph Series* (Vol. 23, pp. 1–35). AGU. https://doi.org/10.1029/gm023p0001

Cottam, M. A., Hall, R., Forster, M., & Boudagher Fadel, M. (2011). Basement character and basin formation in Gorontalo Bay, Sulawesi, Indonesia: New observations from the Togian Islands. In R. Hall, M. A. Cottam, & M. E. J. Wilson (Eds.), *.The SE Asian gateway: History and tectonics of Australia–Asia collision* (Vol. 355(1), pp. 177–202). *Geological Society of London Special Publication*. https://doi.org/10.1144/sp355.9

Crampin, S. (1994). The fracture criticality of crustal rocks. *Geophysical Journal International*, *118*(2), 428–438. https://doi.org/10.1111/j.1365-246x.1994.tb03974.x

Dal Zilio, L., Faccenda, M., & Capitanio, F. (2017). The role of deep subduction in supercontinent breakup. *Tectonophysics*, *746*, 1–13. https://doi.org/10.1016/j.tecto.2017.03.006

Di Leo, J. F., Wookey, J., Hammond, J. O. S., Kendall, J. M., Kaneshima, S., Inoue, H., et al. (2012a). Mantle flow in regions of complex tectonics: Insights from Indonesia. *Geochemistry, Geophysics, Geosystems*, *13*(12), Q12008. https://doi.org/10.1029/2012GC004417

Di Leo, J. F., Wookey, J., Hammond, J. O. S., Kendall, J. M., Kaneshima, S., Inoue, H., et al. (2012b). Deformation and mantle flow beneath the Sangihe subduction zone from seismic anisotropy. *Physics of the Earth and Planetary Interiors*, *194–195*, 38–54. https://doi.org/10.1016/j.pepi.2012.01.008

Dong, M., Lü, C. C., Zhang, J., & Hao, T. (2022). Downgoing plate-buoyancy driven retreat of North Sulawesi Trench: Transition of a passive margin into a subduction zone. *Geophysical Research Letters*, *49*(23), e2022GL101130. https://doi.org/10.1029/2022gl101130

Fauzi, M. F., Anggraini, A., Riyanto, A., Ngadmanto, D., & Suryanto, W. (2021). Crustal thickness estimation in Indonesia using receiver function method. *IOP Conference Series: Earth and Environmental Science*, *873*(1), 012086. https://doi.org/10.1088/1755-1315/873/1/012086

Gérault, M., Becker, T. W., Kaus, B. J. P., Faccenna, C., Moresi, L., & Husson, L. (2012). The role of slabs and oceanic plate geometry in the net rotation of the lithosphere, trench motions, and slab return flow. *Geochemistry, Geophysics, Geosystems*, *13*(4), Q04001. https://doi.org/10.1029/2011GC003934

Greenfield, T., Copley, A. C., Caplan, C., Supendi, P., Widiyantoro, S., & Rawlinson, N. (2021). Crustal deformation and fault strength of the Sulawesi subduction zone. *Tectonics*, *40*(3), e2020TC006573. https://doi.org/10.1029/2020TC006573

Hall, C. E., Fischer, K. M., Parmentier, E. M., & Blackman, D. K. (2000). The influence of plate motions on three-dimensional back arc mantle flow and shear wave. *Journal of Geophysical Research*, *105*(B12), 28009–28033. https://doi.org/10.1029/2000jb900297

Hall, R. (2002). Cenozoic geological and plate tectonic evolution of SE Asia and the SW Pacific: Computer-based reconstructions, model and animations. *Journal of Asian Earth Sciences*, *20*(4), 353–431. https://doi.org/10.1016/S1367-9120(01)00069-4

Hall, R., & Sevastjanova, I. (2012). Australian crust in Indonesia. *Australian Journal of Earth Sciences*, *59*(6), 827–844. https://doi.org/10.1080/08120099.2012.692335

Hall, R., & Spakman, W. (2015). Mantle structure and tectonic history of SE Asia. *Tectonophysics*, *658*, 14–45. https://doi.org/10.1016/j.tecto.2015.07.003

Hayes, G. P., Moore, G. L., Portner, D. E., Hearne, M., Flamme, H., Furtney, M., & Smoczyk, G. M. (2018). Slab2, a comprehensive subduction zone geometry model. *Science*, *88*(6410), 61. https://doi.org/10.1126/science.aat4723

Hoernle, K., Abt, D. L., Fischer, K. M., Nichols, H., Hauff, F., Abers, G., et al. (2008). Geochemical and geophysical evidence for arc-parallel flow in the mantle wedge beneath Costa Rica and Nicaragua. *Nature*, *451*, 1094–1098. https://doi.org/10.1038/nature06550

Honda, S., & Yoshida, T. (2005). Effects of oblique subduction on the 3-D pattern of small-scale convection within the mantle wedge. *Geophysical Research Letters*, *32*(13), L13307. https://doi.org/10.1029/2005gl023106

Hua, Y., Zhao, D., & Xu, Y.-G. (2022). Azimuthal anisotropy tomography of the Southeast Asia subduction system. *Journal of Geophysical Research: Solid Earth*, *127*(2), e2021JB022854. https://doi.org/10.1029/2021JB022854

Huang, Z., Zhao, D., & Wang, L. (2015). P wave tomography and anisotropy beneath Southeast Asia: Insight into mantle dynamics. *Journal of Geophysical Research: Solid Earth*, *120*(7), 5154–5174. https://doi.org/10.1002/2015JB012098

Hutchings, S. J., & Mooney, W. D. (2021). The seismicity of Indonesia and tectonic implications. *Geochemistry, Geophysics, Geosystems*, *22*(9), e2021GC009812. https://doi.org/10.1029/2021GC009812

Jaffe, L. A., Hilton, D. R., Fischer, T. P., & Hartono, U. (2004). Tracing magma sources in an arc–arc collision zone: Helium and carbon isotope and relative abundance systematics of the Sangihe Arc, Indonesia. *Geochemistry, Geophysics, Geosystems*, *5*(4), Q04J10. https://doi.org/10.1029/2003GC000660

Jagoutz, O., Royden, L., Holt, A. F., & Becker, T. W. (2015). Anomalously fast convergence of India and Eurasia caused by double subduction. *Nature Geoscience*, *8*(6), 475–478. https://doi.org/10.1038/ngeo2418

Ji, Y., Yoshioka, S., Manea, V. C., & Manea, M. (2017). Seismogenesis of dual subduction beneath Kanto, Central Japan controlled by fluid release. *Scientific Reports*, *7*(1), 16864. https://doi.org/10.1038/s41598-017-16818-z

Király, Á., Capitanio, F. A., Funiciello, F., & Faccenna, C. (2016). Subduction zone interaction: Controls on arcuate belts. *Geology*, *44*(9), 715–718. https://doi.org/10.1130/G37912.1

Király, Á., Faccenna, C., & Funiciello, F. (2018). Subduction zones interaction around the Adria microplate and the origin of the Apenninic arc. *Tectonics*, *37*(10), 3941–3953. https://doi.org/10.1029/2018TC005211

Király, Á., Funiciello, F., Capitanio, F. A., & Faccenna, C. (2021). Dynamic interactions between subduction zones. *Global and Planetary Change*, *202*, 103501. https://doi.org/10.1016/j.gloplacha.2021.103501

Király, Á., Holt, A. F., Funiciello, F., Faccenna, C., & Capitanio, F. A. (2018). Modeling slab-slab interactions: Dynamics of outward dipping double-sided subduction systems. *Geochemistry, Geophysics, Geosystems*, *19*(3), 693–714. https://doi.org/10.1002/2017GC007199

Kopp, C., Flueh, E. R., & Neben, S. (1999). Rupture and accretion of the Celebes Sea crust related to the North-Sulawesi subduction: Combined interpretation of reflection and refraction seismic measurements. *Geodynamics*, *27*(3), 309–325. https://doi.org/10.1016/s0264-3707(98)00004-0

Kubo, A., & Hiramatsu, Y. (1998). On presence of seismic anisotropy in the asthenosphere beneath continents and its dependence on plate velocity: Significance of reference frame selection. In *Geodynamics of lithosphere & Earth's mantle: Seismic anisotropy as a record of the past and present dynamic processes* (pp. 281–303). Birkhäuser Basel.

Lallemand, S., Font, Y., Bijwaard, H., & Kao, H. (2001). New insights on 3-D plates interaction near Taiwan from tomography and tectonic implications. *Tectonophysics*, *335*(3–4), 229–253. https://doi.org/10.1016/S0040-1951(01)00071-3

León Soto, G., & Valenzuela, R. W. (2013). Corner flow in the Isthmus of Tehuantepec, Mexico inferred from anisotropy measurements using local intraslab earthquakes. *Geophysical Journal International*, *195*(2), 1230–1238. https://doi.org/10.1093/gji/ggt291

Linang, H. T. (2023). Crustal structure and tectonics of Borneo and Sulawesi: Results from receiver function analysis and virtual deep seismic sounding. *Diss. University of Cambridge*.

Liu, C., & Shi, Y. L. (2021). Space-time stress variations on the Palu-Koro fault impacting the 2018 Mw 7.5 Palu earthquake and its seismic hazards. *Geochemistry, Geophysics, Geosystems*, *22*(5), e2020GC009552. https://doi.org/10.1029/2020GC009552

Long, M. D. (2013). Constrains on subduction geodynamics from seismic anisotropy. *Reviews of Geophysics*, *51*(1), 76–112. https://doi.org/10.1002/rog.20008

Long, M. D., & Silver, P. G. (2008). The subduction zone flow field from seismic anisotropy: A global view. *Science*, *319*(5861), 315–318. https://doi.org/10.1126/science.1150809

Long, M. D., & Silver, P. G. (2009). Shear wave splitting and mantle anisotropy: Measurements, interpretations, and new directions. *Surveys in Geophysics*, *30*(4), 407–461. https://doi.org/10.1007/s10712-009-9075-1

Long, M. D., & van der Hilst, R. D. (2005). Upper mantle anisotropy beneath Japan from shear wave splitting. *Physics of the Earth and Planetary Interiors*, *151*(3–4), 206–222. https://doi.org/10.1016/j.pepi.2005.03.003

Long, M. D., & van der Hilst, R. D. (2006). Shear wave splitting from local events beneath the Ryukyu arc: Trench-parallel anisotropy in the mantle wedge. *Physics of the Earth and Planetary Interiors*, *155*(3–4), 300–312. https://doi.org/10.1016/j.pepi.2006.01.003

Long, M. D., & Wirth, E. A. (2013). Mantle flow in subduction systems: The mantle wedge flow field and implications for wedge processes. *Journal of Geophysical Research: Solid Earth*, *118*(2), 583–606. https://doi.org/10.1002/jgrb.50063

Lynner, C., & Long, M. D. (2013). Sub-slab seismic anisotropy and mantle flow beneath the Caribbean and Scotia subduction zones: Effects of slab morphology and kinematics. *Earth and Planetary Science Letters*, *361*, 367–378. https://doi.org/10.1016/j.epsl.2012.11.007

Lynner, C., & Long, M. D. (2014). Sub-slab anisotropy beneath the Sumatra and circum-Pacific subduction zones from source-side shear wave splitting observations. *Geochemistry, Geophysics, Geosystems*, *15*(6), 2262–2281. https://doi.org/10.1002/2014GC005239

Marson-Pidgeon, K., & Savage, M. K. (1997). Frequency-dependent anisotropy in Wellington, New Zealand. *Geophysical Research Letters*, *24*(24), 3297–3300. https://doi.org/10.1029/97gl03274

Marson-Pidgeon, K., & Savage, M. K. (2004). Shear-wave splitting variations across an array in the southern North Island, New Zealand. *Geophysical Research Letters*, *31*(21), L21602. https://doi.org/10.1029/2004GL021190

Matharu, G., Bostock, M. G., Christensen, N. I., & Tromp, J. (2014). Crustal anisotropy in a subduction zone forearc: Northern Cascadia. *Journal of Geophysical Research: Solid Earth*, *119*(9), 7058–7078. https://doi.org/10.1002/2014jb011321

Natawidjaja, D. H., Daryono, M. R., Prasetya, G., Liu, P. L., Hananto, N. D., Kongko, W., et al. (2021). The 2018 M w7. 5 Palu 'super-shear'earthquake ruptures geological fault's multisegment separated by large bends: Results from integrating field measurements, LiDAR, swath bathymetry and seismic-reflection data. *Geophysical Journal International*, *224*(2), 985–1002. https://doi.org/10.1093/gji/ggaa498

Restivo, A., & Helffrich, G. (1999). Teleseismic shear wave splitting measurements in noise environments. *Geophysical Journal International*, *137*(3), 821–830. https://doi.org/10.1046/j.1365-246x.1999.00845.x

Ribe, N. M. (1989). Seismic anisotropy and mantle flow. *Journal of Geophysical Research*, *94*(B4), 4213–4223. https://doi.org/10.1029/jb094ib04p04213

Roy, S. K., Ravi Kumar, M., & Davuluri, S. (2017). Anisotropy in subduction zones: Insights from new source side S-wave splitting measurements from India. *Journal of Geophysical Research: Solid Earth*, *115*(8), 6454–6472. https://doi.org/10.1002/2017JB014314

Savage, M. K., Fischer, K. M., & Hall, C. E. (2004). Strain modelling, seismic anisotropy and coupling at strike-slip boundaries: Applications in New Zealand and the San Andreas Fault. *Geological Society London Special Publications*, *227*(1), 9–39. https://doi.org/10.1144/gsl.sp.2004.227.01.02

Savage, M. K., Wessel, A., Teanby, N., & Hurst, T. (2010). Automatic measurement of shear wave splitting and applications to time varying anisotropy at Mt. Ruapehu volcano, New Zealand. *Journal of Geophysical Research*, *115*(B12), B12321. https://doi.org/10.1029/2010JB007722

Silver, P. G. (1996). Seismic anisotropy beneath the continents: Probing the depths of geology. *Annual Review of Earth and Planetary Sciences*, *24*(1), 385–432. https://doi.org/10.1146/annurev.earth.24.1.385

Silver, P. G., & Chan, W. W. (1991). Shear wave splitting and subcontinental mantle deformation. *Journal of Geophysical Research*, *96*(B10), 16429–16454. https://doi.org/10.1029/91jb00899

Smith, G. P., Wiens, D. A., Fischer, K. M., Dorman, L. M., Webb, S. C., & Hildebrand, J. A. (2001). A complex pattern of mantle flow in the Lau backarc. *Science*, *292*(5517), 713–716. https://doi.org/10.1126/science.1058763

Socquet, A., Simons, W., Vigny, C., McCaffrey, R., Subarya, C., Sarsito, D., et al. (2006). Microblock rotations and fault coupling in SE Asia triple junction (Sulawesi, Indonesia) from GPS and earthquake slip vector data. *Journal of Geophysical Research*, *111*(B8), B08409. https://doi.org/10.1029/2005jb003963

Song, T., Hao, T., Zhang, J., Cao, L., & Dong, M. (2022). Numerical modeling of North Sulawesi subduction zone: Implications for the east–west differential evolution. *Tectonophysics*, *822*, 229172. https://doi.org/10.1016/j.tecto.2021.229172

Tatsumi, Y., Murasaki, M., Arsadi, E. M., & Nohda, S. (1991). Geochemistry of Quaternary lavas from NE Sulawesi: Transfer of subduction components into the mantle wedge. *Contributions to Mineralogy and Petrology*, *107*(2), 137–149. https://doi.org/10.1007/bf00310703

Teanby, N., Kendall, J. M., & Van der Baan, M. (2004). Automation of shear-wave splitting measurements using cluster analysis [Software]. *Bulletin of the Seismological Society of America*, *94*(2), 453–463. https://doi.org/10.1785/0120030123

Vignaroli, G., Faccenna, C., Jolivet, L., Piromallo, C., & Rossetti, F. (2008). Subduction polarity reversal at the junction between the Western Alps and the Northern Apennines, Italy. *Tectonophysics*, *450*(1–4), 34–50. https://doi.org/10.1016/j.tecto.2008.10.01

Wada, I. (2021). A simple picture of mantle wedge flow patterns and temperature variation. *Journal of Geodynamics*, *146*, 101848. https://doi.org/10.1016/j.jog.2021.101848

Walpersdorf, A., Vigny, C., Subarya, C., & Manurung, P. (1998). Monitoring of the Palu-Koro Fault (Sulawesi) by GPS. *Geophysical Research Letters*, *25*(13), 2313–2316. https://doi.org/10.1029/98gl01799

Walsh, E., Arnold, R., & Savage, M. K. (2013). Silver and Chan revisited. *Journal of Geophysical Research: Solid Earth*, *118*(10), 5500–5515. https://doi.org/10.1002/jgrb.50386

Wang, L., & He, X. (2020). Seismic anisotropy in the java-banda and philippine subduction zones and its implications for the mantle flow system beneath the Sunda Plate. *Geochemistry, Geophysics, Geosystems*, *21*(4), 1095. https://doi.org/10.1029/2019gc008658

Wehner, D., Blom, N., Rawlinson, N., Böhm, C., Miller, M. S., Supendi, P., & Widiyantoro, S. (2022). SASSY21: A 3-D seismic structural model of the lithosphere and underlying mantle beneath Southeast Asia from multi-scale adjoint waveform tomography. *Journal of Geophysical Research: Solid Earth*, *127*(3), e2021JB022930. https://doi.org/10.1029/2021JB022930

Wessel, A. (2010). *Automatic shear wave splitting measurements at Mt. Ruapehu volcano. Master's thesis*. Victoria University of Wellington.

Wessel, P., & Smith, W. H. F. (1991). Free software helps map and display data [Software]. *Eos Trans. AGU*, *72*(41), 441–446. https://doi.org/10.1029/90EO00319

Wolfe, C. J., & Silver, P. G. (1998). Seismic anisotropy of oceanic upper mantle: Shear wave splitting methodologies and observations. *Journal of Geophysical Research*, *103*(B1), 749–771. https://doi.org/10.1029/97jb02023

Wüstefeld, A., Bokelmann, G., Zaroli, C., & Barruol, G. (2008). SplitLab: A shear-wave splitting environment in Matlab. *Computers & Geosciences*, *34*(5), 515–528. https://doi.org/10.1016/j.cageo.2007.08.002

Yuan, H., Romanowicz, B., Fischer, K. M., & Abt, D. (2011). 3-D shear wave radially and azimuthally anisotropic velocity model of the North American upper mantle. *Geophysical Journal International*, *184*(3), 1237–1260. https://doi.org/10.1111/j.1365-246x.2010.04901.x

Zenonos, A., De Siena, L., Widiyantoro, S., & Rawlinson, N. (2019). P and S wave travel time tomography of the SE Asia-Australia collision zone. *Physics of the Earth and Planetary Interiors*, *293*, 106267. https://doi.org/10.1016/j.pepi.2019.05.010

Zietlow, D. W., Sheehan, A. F., Molnar, P. H., Savage, M. K., Hirth, G., Collins, J. A., & Hager, B. H. (2014). Upper mantle seismic anisotropy at a strike-slip boundary: South Island, New Zealand. *Journal of Geophysical Research: Solid Earth*, *119*(2), 1020–1040. https://doi.org/10.1002/2013JB010676